Available online at www.sciencedirect.com
SCIENCE DIRECT®
Journal of Computational Physics 207 (2005) 282–308
JOURNAL OF COMPUTATIONAL PHYSICS
www.elsevier.com/locate/jcp

Preconditioning for incompressible flows with free-surfaces and two-fluid interfaces

B.T. Helenbrook *

Mechanical and Aeronautical Engineering Department, Clarkson University, Potsdam, NY 13699-5725, USA

Received 24 May 2004; received in revised form 9 November 2004; accepted 11 January 2005
Available online 7 April 2005

Abstract

We investigate preconditioners for solving steady or implicit-unsteady arbitrary-Lagrangian–Eulerian moving-mesh formulations of incompressible free-surface and interfacial flow problems. The solution for the flow is obtained using the artificial compressibility method combined with a multigrid cycle. To find the surface positions in a free-surface problem, we use an iteration that is quasi-physical with the position of the free-surface driven by the kinematic condition. By modifying the fluxes through the free-surface and also using an iterative free-surface time step that is different from the flow time-step, we are able to obtain convergence rates that are almost indistinguishable from those of a flow without a free-surface. This is true in the limits of both large and small surface stresses such as gravity or surface tension and also for all flow conditions (high or low Reynolds number or small implicit Courant–Friedrichs–Lewy number). For interfacial flows, the free-surface preconditioner is extended by using a mass averaging technique. The iterative flow time-step at the interface is a mass average of the time step for the flow conditions on either side of the interface and the iterative time step for the kinematic condition is also based on mass-average quantities. We verify that this technique produces the correct results in the limits of identical fluids or a free-surface flow. We also verify that it produces well-conditioned results when the characteristic time scales of the two fluids are very different.

PACS: 65B99; 76T10; 76B07; 76D99

Keywords: Preconditioning; Incompressible flow; Free-surface flow; Interfacial flow; Artificial compressibility; Multigrid

* Tel.: +1 315 268 2204.
E-mail address: helenbrk@clarkson.edu.
URL: http://www.clarkson.edu/mae/faculty/helenbrook.html.

0021-9991/$ - see front matter © 2005 Published by Elsevier Inc.
doi:10.1016/j.jcp.2005.01.012

1. Introduction

Arbitrary-Lagrangian–Eulerian (ALE) moving-mesh techniques have been used to simulate both unsteady and steady incompressible free-surface and interfacial flow problems over a wide range of Reynolds, Weber, and Froude numbers. Examples range from flow over ship hulls at high Reynolds number [1,2] to simulations of falling liquid droplets at low Reynolds number [3,4]. For the ship problem both high- and low-Froude number conditions are relevant, and for the droplet high- and low-Weber number conditions are also important. Although ALE techniques have been successfully used to simulate all of these conditions, there is no preferred method for solving the non-linear system of equations that results from an ALE discretization. As we discuss in the following, various methods have been used, and there is little understanding of when each method works or which method works best.

Several different iterative techniques have been proposed to solve the equations governing the positions of the surfaces in ALE formulations. These can be divided into two main categories: In the first, the error in the kinematic condition (the condition that the mass flux through the interface is zero) is used to drive the iteration for the position of the interface [1,5–10]. This approach has been combined with various flow solvers including artificial compressibility solvers [1,10], pressure-projection solvers [7,11,12], and stream-function-vorticity [13] approaches because it corresponds to a physical evolution of the surface position. The other technique is to drive the position of the surface using the error in the normal-stress boundary condition [3,7,14,15].

There has been little analysis of either of these two approaches. In general, the normal stress approach is favored when the surface stresses either from surface tension or gravity are large [7]. In this paper, we focus on the kinematic condition technique because it is quasi-physical and is also easier to implement than the stress-driven technique. The goal is to develop an efficient iteration that can be used under all flow conditions. Although the surface preconditioner we develop is designed to be combined with a artificial-compressibility multigrid iteration, many of the results and analysis techniques can be generalized for other flow solvers as well.

The paper is divided into two main topics: the optimization of the free-surface preconditioner and the optimization of the interfacial flow preconditioner. Section 2 presents the governing equations for the flow and free-surface. For the purpose of analysis, these equations are linearized around the state of a flat free surface with a parallel uniform flow. Section 3 gives a discrete implementation of the linearized equations that is vertex based on a structured mesh. In Section 4, we describe the artificial compressibility iteration used to obtain the flow solution. Section 5 gives a continuous analysis of the coupled free-surface/artificial compressibility problem. This gives insight into the expected behavior of the discrete free-surface problem. We then describe the techniques used to analyze the discrete problem and optimize the free-surface preconditioner in the limits of high and low Reynolds number and small implicit Courant–Friedrichs–Lewy (CFL) number as well as large and small Froude and Weber numbers. Numerical tests are performed to confirm that the preconditioner gives good results under all conditions. Section 6 examines the interfacial problem. We give a discrete formulation for both inviscid and viscous interfacial flows and then discuss the modifications needed to the flow and free-surface preconditioners to obtain good results for interfacial problems. Predictions from the analysis are numerically tested to show the effectiveness of the interfacial preconditioner. Section 7 then concludes the paper.

2. Continuous problem

The problem we use to analyze different preconditioning schemes is an infinite-depth free-surface flow. The free surface is positioned at $y = 0$, and the domain extends to negative infinity in the y-direction. A gravitational force acts in the negative y-direction with gravitational acceleration g. Surface tension, σ, is also included. The flow is assumed to be incompressible with a constant fluid density, ρ, and dynamic

viscosity, μ. Because we are interested in analyzing an ALE moving-mesh discretization of this problem, the governing equations are written in moving curvilinear coordinates, $x(\xi,\eta,\tau)$, $y(\xi,\eta,\tau)$, and $\tau = t$, where x and y are the two-dimensional Cartesian coordinates, t is the time, and ξ, η, and τ are the independent curvilinear coordinates. In the following, subscripts of the curvilinear coordinates or the physical coordinates denote differentiation.

In unsteady curvilinear coordinates, the incompressible Navier–Stokes equations are

$$\frac{\partial J[\rho,\rho U,\rho V]^{\mathrm{T}}}{\partial\tau}+\frac{\partial}{\partial\xi}J(\xi_x\vec{\mathrm{p}}+\xi_y\vec{\mathrm{q}})+\frac{\partial}{\partial\eta}J(\eta_x\vec{\mathrm{p}}+\eta_y\vec{\mathrm{q}})=\frac{\partial\vec{\mathrm{r}}}{\partial\xi}+\frac{\partial\vec{\mathrm{s}}}{\partial\eta}+[0,0,\rho gJ]^{\mathrm{T}}. \tag{1}$$

The Jacobian, J, and the inverse metrices ξ_x, ξ_y, η_x, and η_y are determined from the linearization of the curvilinear transformation. U and V are the flow velocity components in the x- and y-coordinate directions, respectively.

The inviscid fluxes, $\vec{\mathrm{p}}$ and $\vec{\mathrm{q}}$, are given by

$$\vec{\mathrm{p}}=\begin{Bmatrix}\rho(U-x_\tau)\\ \rho U(U-x_\tau)+P\\ \rho V(U-x_\tau)\end{Bmatrix},\qquad \vec{\mathrm{q}}=\begin{Bmatrix}\rho(V-y_\tau)\\ \rho U(V-y_\tau)\\ \rho V(V-y_\tau)+P\end{Bmatrix}, \tag{2}$$

where P is the pressure.

$\vec{\mathrm{r}}$ and $\vec{\mathrm{s}}$ are the components of the viscous stress tensor in curvilinear coordinates

$$\vec{\mathrm{r}}=\left\{\mathrm{K}^{\xi\xi}\frac{\partial}{\partial\xi}+\mathrm{K}^{\xi\eta}\frac{\partial}{\partial\eta}\right\}[0,U,V]^{\mathrm{T}},\quad \vec{\mathrm{s}}=\left\{\mathrm{K}^{\eta\xi}\frac{\partial}{\partial\xi}+\mathrm{K}^{\eta\eta}\frac{\partial}{\partial\eta}\right\}[0,U,V]^{\mathrm{T}}. \tag{3}$$

The matrices $\mathrm{K}^{m\,n}$ with $m,n=\xi,\eta$ have the general form

$$\mathrm{K}^{mn}=\mu J\begin{bmatrix}0 & 0 & 0\\ 0 & (2m_xn_x+m_yn_y) & m_yn_x\\ 0 & m_xn_y & (2m_yn_y+m_xn_x)\end{bmatrix}. \tag{4}$$

For convenience, we also introduce the total flux vectors in the ξ and η directions, $\vec{\mathrm{e}}=J(\xi_x\vec{\mathrm{p}}+\xi_y\vec{\mathrm{q}})-\vec{\mathrm{r}}$ and $\vec{\mathrm{f}}=J(\eta_x\vec{\mathrm{p}}+\eta_y\vec{\mathrm{q}})-\vec{\mathrm{s}}$.

For the analysis, we specialize the above formulation to the case of a nearly planar free-surface located at $y=0$. We assume that the moving coordinates are of the following specific form:

$$x=\Delta x\xi,\quad y=\Delta y\eta+h(\xi,\tau), \tag{5}$$

where Δx and Δy are the horizontal and vertical mesh spacings. This corresponds to a uniform mesh in the x-direction. The y mesh positions are also uniformly spaced, but with a vertical offset, $h(\xi,\tau)$, for any column of vertices. h is the height of the free surface, thus any vertical column of mesh points translates rigidly with the position of the free surface. The results presented in the following are insensitive to the particular choice of mesh movement scheme.

In these coordinates, Eq. (1) becomes

$$\left(\Delta x\Delta y[\rho,\rho U,\rho V]^{\mathrm{T}}\right)_\tau+(\Delta y\vec{\mathrm{p}})_\xi+(\Delta x\vec{\mathrm{q}}-h_\xi\vec{\mathrm{p}})_\eta=\vec{\mathrm{r}}_\xi+\vec{\mathrm{s}}_\eta+[0,0,\rho g\Delta x\Delta y]^{\mathrm{T}}. \tag{6}$$

The inviscid fluxes simplify to

$$\vec{\mathrm{p}}=\begin{Bmatrix}\rho U\\ \rho U^2+P\\ \rho VU\end{Bmatrix},\qquad \vec{\mathrm{q}}=\begin{Bmatrix}\rho(V-h_\tau)\\ \rho U(V-h_\tau)\\ \rho V(V-h_\tau)+P\end{Bmatrix}. \tag{7}$$

The specific form of the viscous fluxes, $\vec{r}$ and $\vec{s}$, can be determined from Eqs. (3) and (4). The viscous fluxes involve both the flow velocities and the free-surface height because of the movement of the mesh with the free surface. A linearized form is given in the following.

To analyze the above-governing equations, we linearize around the steady-state solution of a uniform horizontal velocity, u_∞, a flat free surface, and the hydrostatic pressure, $P = -\rho g y$. The perturbation to the horizontal and vertical flow velocity, pressure, and free-surface height are given by u, v, p, and h, respectively. The linearization of the governing equations is given by

$$\Delta x \Delta y \begin{bmatrix} 0 & 0 & 0 \\ 0 & 1 & 0 \\ 0 & 0 & 1 \end{bmatrix} w_\tau + \vec{e}_\xi + \vec{f}_\eta = 0, \tag{8}$$

where

$$w = \begin{bmatrix} p \\ u \\ v \end{bmatrix}, \tag{9}$$

the linearized total fluxes, $\vec{e}$ and $\vec{f}$, are given by the following relations:

$$\vec{e} = A_x w - N_{xx} w_\xi - N_{xy} w_\eta, \tag{10}$$

$$\vec{f} = A_y w - A_y \begin{bmatrix} 0 \\ 0 \\ h_\tau \end{bmatrix} - h_\xi \begin{bmatrix} \rho\beta u_\infty \\ u_\infty^2 \\ 0 \end{bmatrix} - N_{yx} w_\xi - N_{yy} w_\eta, \tag{11}$$

$$A_x = \Delta y \begin{bmatrix} 0 & \rho\beta & 0 \\ 1/\rho & 2u_\infty & 0 \\ 0 & 0 & u_\infty \end{bmatrix}, \qquad A_y = \Delta x \begin{bmatrix} 0 & 0 & \rho\beta \\ 0 & 0 & u_\infty \\ 1/\rho & 0 & 0 \end{bmatrix}, \tag{12}$$

$$N_{xx} = \frac{\nu \Delta y}{\Delta x} \begin{bmatrix} 0 & 0 & 0 \\ 0 & 2 & 0 \\ 0 & 0 & 1 \end{bmatrix}, \qquad N_{xy} = \nu \begin{bmatrix} 0 & 0 & 0 \\ 0 & 0 & 0 \\ 0 & 1 & 0 \end{bmatrix}, \tag{13}$$

$$N_{yx} = \nu \begin{bmatrix} 0 & 0 & 0 \\ 0 & 0 & 1 \\ 0 & 0 & 0 \end{bmatrix}, \qquad N_{yy} = \frac{\nu \Delta x}{\Delta y} \begin{bmatrix} 0 & 0 & 0 \\ 0 & 1 & 0 \\ 0 & 0 & 2 \end{bmatrix}. \tag{14}$$

In addition to linearizing the governing equations, we have also divided the momentum equations by ρ and multiplied the continuity equation by an artificial compressibility constant β which is described in the flow preconditioning section. The matrices denoted with N are the linearized form of Eq. (4), where μ is replaced by the kinematic viscosity ν because we have divided by ρ. The second and third terms of $\vec{f}$ are not functions of η, and thus do not affect Eq. (8). However, we keep these terms in the formulation because it makes the following discussion of the boundary conditions simpler.

The linearized free-surface boundary conditions specify the flux of mass and the stresses on the free surface. These conditions can be written compactly as

$$\vec{\mathrm{f}}|_{y=h} = \left[0, 0, \Delta x g h - \frac{\sigma}{\rho \Delta x} h_{\xi\xi}\right]^{\mathrm{T}}. \tag{15}$$

The first two components of this equation enforce the condition that the total flux of mass and the total flux of horizontal momentum through the free surface are zero. The last component states that the total flux of vertical momentum is determined by the applied stress to the free surface. This can be seen more clearly be expanding $\vec{\mathrm{f}}$. The three equations can then be shown to be curvilinear-coordinate forms of: the kinematic condition,

$$\Delta x \beta \rho \left((v - h_\tau) - u_\infty \frac{h_\xi}{\Delta x} \right) = 0, \tag{16}$$

which enforces the fact that there is no convective flux through the free surface, a linear combination of the kinematic condition and the shear stress condition,

$$\frac{\Delta x}{\rho} \left[\rho u_\infty \left((v - h_\tau) - u_\infty \frac{h_\xi}{\Delta x} \right) - \mu \left(\frac{v_\xi}{\Delta x} + \frac{u_\eta}{\Delta y} \right) \right] = 0, \tag{17}$$

which makes the shear stress zero, and the normal stress condition,

$$\frac{\Delta x}{\rho} \left[p - 2\mu \frac{v_\eta}{\Delta y} = \rho g h - \sigma \frac{h_{\xi\xi}}{\Delta x^2} \right]. \tag{18}$$

For the boundary at $y = -\infty$, we require that the flow perturbations decay to zero. In the x-direction, the domain is assumed to be infinite.

3. Discrete governing equations

The above equations are made discrete in time using an implicit Euler backwards difference scheme with time step, $\Delta\tau$. The backwards difference terms from previous physical time steps are ignored because they are constant during the iterative procedure and have no effect on the conditioning of the system. The spatial discretization is vertex based on a structured quadrilateral mesh. The following is the discrete form of the linearized governing equations:

$$\Delta x \Delta y \begin{bmatrix} 0 & 0 & 0 \\ 0 & \Delta\tau^{-1} & 0 \\ 0 & 0 & \Delta\tau^{-1} \end{bmatrix} w_{j,k} + (\vec{\mathrm{e}}_{j+1/2,k} - \vec{\mathrm{e}}_{j-1/2,k}) + (\vec{\mathrm{f}}_{j,k+1/2} - \vec{\mathrm{f}}_{j,k-1/2}) = 0, \tag{19}$$

$$\begin{aligned} \vec{\mathrm{e}}_{j-1/2,k} = {} & A_x \frac{w_{j,k} + w_{j-1,k}}{2} - \frac{1}{2} D_x (w_{j,k} - w_{j-1,k}) - N_{xx} (w_{j,k} - w_{j-1,k}) \\ & - N_{xy} \frac{w_{j,k+1} - w_{j,k-1} + w_{j-1,k+1} - w_{j-1,k-1}}{4}, \end{aligned} \tag{20}$$

$$\begin{aligned} \vec{\mathrm{f}}_{j,k-1/2} = {} & A_y \frac{w_{j,k} + w_{j,k-1}}{2} - \frac{1}{2} D_y (w_{j,k} - w_{j,k-1}) - N_{yx} \frac{w_{j+1,k} - w_{j-1,k} + w_{j+1,k-1} - w_{j-1,k-1}}{4} \\ & - N_{yy} (w_{j,k} - w_{j,k-1}), \end{aligned} \tag{21}$$

j and k are the horizontal and vertical node indices, respectively. $k = 0$ is the free surface and k decreases with depth below the free surface. D_x and D_y are artificial dissipation matrices. These are given by

$$D_x = \begin{bmatrix} 1 & 0 & 0 \\ 0 & u_\infty/\sqrt{\beta/3} & 0 \\ 0 & 0 & u_\infty/\sqrt{\beta/3} \end{bmatrix} |A_x|, \tag{22}$$

$$D_y = \begin{bmatrix} 1 & 0 & 0 \\ 0 & u_\infty/\sqrt{\beta/3} & 0 \\ 0 & 0 & u_\infty/\sqrt{\beta/3} \end{bmatrix} |A_y|. \tag{23}$$

$|A|$ is defined as $V|\Lambda|V^{-1}$, where V and Λ are determined from the eigenvalue problem $A\ V = V\Lambda$. The reason for choosing this form of the dissipation matrices is discussed in Section 4. Although the spatial and temporal schemes are both only first-order accurate, they provide enough insight to determine an optimal preconditioner.

Because the spatial discretization is vertex based, there are values of u,v, and p located on the free surface. The free-surface boundary conditions are enforced by applying conservation of mass and momentum to a half volume surrounding the nodes on the free surface. The flux at the free surface is given by Eq. (15) with the normal stress approximated by $\rho g h_j - \sigma(h_{j+1} - 2h_j + h_{j-1})/\Delta x^2$. The equations governing the free-surface nodes are then

$$\frac{\Delta x \Delta y}{2} \begin{bmatrix} 0 & 0 & 0 \\ 0 & \Delta\tau^{-1} & 0 \\ 0 & 0 & \Delta\tau^{-1} \end{bmatrix} w_{j,k} + \frac{1}{2}(\vec{e}_{j+1/2,0} - \vec{e}_{j-1/2,0}) + \left[0, 0, \Delta x g h_j - \frac{\sigma}{\rho \Delta x}(h_{j+1} - 2h_j + h_{j-1})\right]^{\mathrm{T}} - \vec{f}_{j,-1/2} = 0. \tag{24}$$

These equations are not quite correct because the $N_{xy} w_\eta$ term in the $\vec{e}_{j+1/2,0}$ and $\vec{e}_{j-1/2,0}$ fluxes has a dependence on $k+1$ (see Eq. (20)). To eliminate this dependence, these fluxes are calculated using a one-sided stencil

$$-N_{xy} \frac{w_{j,0} - w_{j,-1} + w_{j-1,0} - w_{j-1,-1}}{2}. \tag{25}$$

This is then well defined at the free surface. Notice that p is allowed to be an independent variable at the free surface which is solved for by enforcing conservation. This implementation of the free-surface boundary condition arises naturally in ALE finite-volume discretizations and also in ALE finite-element discretizations where the convective terms are integrated by parts.

The evolution of h is determined by the kinematic condition. The discrete linear form of the kinematic boundary condition is given by

$$\Delta x \left(\frac{h_j}{\Delta\tau} - v_j \right) + u_\infty \frac{h_{j+1} - h_{j-1}}{2} - |u_\infty| \frac{h_{j+1} - 2h_j + h_{j-1}}{2} = 0. \tag{26}$$

This is an upwind discretization based on the free-stream velocity, and we again have used a one step backwards-difference in time and ignored the terms from previous time steps.

4. Flow preconditioning

The iteration used to solve the flow equations is based on the artificial compressibility method [16]. The following equation defines this iteration:

$$\frac{\Delta x \Delta y}{\Delta \tau^*} \frac{\partial w_{j,k}}{\partial \tau^*} + R_{j,k}(w) = 0, \tag{27}$$

where $R_{j,k}(w)$ is the residual error in Eq. (19) at the point j,k evaluated using the current estimate of the solution. This residual is used to drive a pseudo-time evolution in τ^*. When this evolution reaches steady state, the residual is zero and we have solved the discrete equations. This is the simplest form for an artificial compressibility conditioner. There are other slightly more complex forms, which are discussed in [17] and also [18].

There are two parameters in this iterative scheme, $\Delta\tau^*$ and β. The choice of these parameters can strongly affect the convergence rate of the system. We use the values determined in the analysis given in [19]. These are given by

$$\beta = 3(U^2 + V^2) + (\max(\Delta x, \Delta y)/(2\Delta\tau) + 2\nu/\max(\Delta x, \Delta y))^2 \tag{28}$$

and

$$1/\Delta\tau^* = 2\left(U + \sqrt{U^2 + \beta}\right)/\Delta x + 2\left(V + \sqrt{V^2 + \beta}\right)/\Delta y + \Delta\tau^{-1} + 8\nu(1/\Delta x^2 + 1/\Delta y^2). \tag{29}$$

These parameters have been optimized using a model problem similar to the one used here except without the free surface. They should give good convergence rates for all limiting flow conditions, including Stokes flow, inviscid flow, and small implicit CFL number ($\Delta\tau u_\infty/\Delta x$).

The dissipation matrices, D_x and D_y, shown in Eqs. (22) and (23) are based on the characteristics of the artificial compressibility system. In the inviscid limit, the matrix pre-multiplying $|A_x|$ and $|A_y|$ is the identity matrix and the scheme is a first-order accurate upwind discretization. For Stokes flow conditions and small CFL numbers, the premultiplication matrix reduces the magnitude of the dissipation from that of a characteristic upwind discretization. This was determined to be necessary in [19] by comparing to the streamwise-upwind-Petrov–Galerkin (SUPG) stabilized finite-element scheme of Brooks and Hughes [20], which gives optimal accuracy for incompressible flow.

In practice, an explicit Runge–Kutta (RK) scheme [21] is often used to update the solution in τ^* and the iteration is combined with a multigrid cycle to achieve good convergence rates [1,22,10]. For the purpose of identifying an optimal free-surface preconditioner, it is adequate to analyze the eigenvalues of the semi-discrete system. In the optimization, we concentrate on the conditioning of the high-wave number modes so that the relaxation scheme will perform well in a multigrid cycle. We note that for flows without a free surface, reference [19] shows that this iterative scheme gives good results for Stokes flow and for small CFL number problems. For the inviscid limit, the convergence rate is not as good. This problem will be apparent in our numerical tests of the free-surface preconditioner, however it does not invalidate the analysis of the free-surface preconditioner.

5. Free-surface preconditioning

We now examine the free-surface problem. As mentioned in the introduction, there are two main types of iterative approaches for solving free-surface problems. In the first, the free surface position is driven by the residual of the kinematic condition [1,5–10]. This approach has dynamics similar to the physical system. In the second, the free-surface position is driven by the imbalance in the normal stress at the free surface [3,7,14,15]. Because the first approach is more physical and also easier to implement than the second, we determine whether this approach can be well conditioned in all limits. The form for the preconditioner is given by

$$\frac{\Delta x}{\Delta \tau^*_{fs}} \frac{\partial h_j}{\partial \tau^*} + R_{fs,j}(w,h) = 0, \tag{30}$$

where $R_{fs,j}$ is the residual of the kinematic equation, Eq. (26) at the point j. $\Delta\tau^*_{fs}$ is a time step for the free surface which may be different than $\Delta\tau^*$. The values of u, v, and p at the free surface are driven in exactly the same manner as the rest of the flow which makes this easy to implement.

5.1. Analytic results

To understand this problem, it is helpful to begin with an examination of the spatially continuous form of the artificial compressibility iteration and free-surface iteration (Eqs. (27) and (30)). The spatially continuous form of the discrete residual operators in these equations is given by Eq. (8) for the flow and Eq. (16) for the kinematic condition except that the physical time derivative operator is replaced by $1/\Delta\tau$. Eq. (16) is also divided by $\rho\beta$ to put it in the same form as the discrete kinematic condition (Eq. (26)). We assume a value of unity for $\Delta\tau^*$ and $\Delta\tau^*_{fs}$. In this case, τ^* is a dimensional time. The boundary conditions are those given in the section describing the continuous problem. Analytic results can be obtained for this problem that give us insight into the fully discrete system.

We begin with the inviscid case. A Fourier transform is performed in the x-direction which eliminates all the spatial derivatives in x. We then substitute $\hat{w}(k_x, y, t) = \hat{w}(k_x, y)e^{\lambda\tau^*}$. For any wavenumber k_x, this leaves us with a linear system of three ordinary differential equations in y which has λ and k_x as parameters. This system has the form

$$\left(I\lambda + \frac{1}{\Delta\tau}\begin{bmatrix}0 & 0 & 0\\ 0 & 1 & 0\\ 0 & 0 & 1\end{bmatrix} - \mathrm{i}k_x A_x\right)\hat{w} + A_y\frac{\partial\hat{w}}{\partial y} = 0. \tag{31}$$

Assuming exponential behavior in y results in a generalized eigenvalue problem for the spatial decay or growth rates in y. Assuming that the temporal eigenvalue λ, is in the left half of the complex plane, we find one eigenmode that is constant in y, one that exponentially decays as y goes to negative infinity, and one that exponentially grows as y goes to negative infinity. Applying the condition that the perturbations decay at negative infinity leaves us with one eigenmode. The form and spatial decay rate of this eigenmode is a function of λ and k_x.

At the free surface, we have two constraints, namely the kinematic condition and the normal stress condition. After application of the Fourier transform, the kinematic condition becomes

$$(\lambda + 1/\Delta\tau - ik_x u_\infty)\hat{h} - \hat{v} = 0 \tag{32}$$

and the normal stress condition becomes

$$\hat{p} = (\rho g + \sigma k_x^2)\hat{h}. \tag{33}$$

The Fourier transform of the normal stress condition shows that for any wavenumber, we do not have to separately investigate surface tension and gravity effects. The only thing that is important is the magnitude of $(\rho g + \sigma k_x^2)$. For simplicity, in the following, we set σ to zero and only examine the effect of gravity.

Substituting the exponentially decaying eigenmode into the normal stress condition and eliminating h with Eq. (32) gives a compatibility condition that determines λ. For inviscid flow, a totally general solution for λ can be found as function of $\Delta\tau$, u_∞, β, and g. This expression is rather lengthy so we focus only on certain limits. When $1/\Delta\tau = 0$, the following expression for λ holds:

$$\lambda = \mathrm{i}k_x u_\infty \pm \sqrt{-\frac{g\left(-g + \sqrt{g^2 + 4k_x^2\beta u_\infty^2 + 4k_x^2\beta^2}\right)}{2\beta}}. \tag{34}$$

When $g = 0$, λ is $ik_x u_\infty$. In this limit, any free-surface oscillation is convected by the free-stream velocity u_∞ and therefore oscillates with a frequency of $k_x u_\infty$. We expect the free-surface problem to be well conditioned in this limit because the free-surface eigenvalue is similar in magnitude to the flow eigenvalues.

A good check on the analysis is the limit of β going to infinity. This drives the artificial speed of sound to infinity and should reproduce classical results for incompressible flows. In the limit of β going to infinity, we arrive at

$$\lambda = ik_x u_\infty \pm i\sqrt{k_x g}, \tag{35}$$

which is exactly the classical result for the oscillation of a free-surface wave. This shows that if a fully incompressible algorithm is used to find steady-state solutions, there is an additional stability constraint proportional to the square root of the gravitational constant. For problems with strong gravitational or surface tension effects, this can seriously limit the rate of convergence to steady state.

When β is fixed and we take the limit of g going to infinity, we obtain the following expression for λ:

$$\lambda = ik_x\left(u_\infty \pm \sqrt{u_\infty^2 + \beta}\right). \tag{36}$$

In this case, the oscillation rate is determined by the artificial speed of sound in the x-direction. (The artificial speed of sound in the x-direction is $\sqrt{u_\infty^2 + \beta}$.) This value does not increase with g. Thus, when using the artificial compressibility method, there should not be any additional time step constraint as g goes to infinity. Unfortunately, as we shall see later, this does not turn out to be true because of the method of implementing the boundary conditions in the discrete system.

A final case is when $1/\Delta\tau$ is not equal to zero, but instead approaches infinity. Using the optimal value for β, we arrive at the following expression for λ:

$$\lambda = \Delta\tau^{-1}. \tag{37}$$

In this limit, we expect that the system will be well conditioned because the characteristic free-surface rate is similar in magnitude to the flow eigenvalues.

For the viscous case, even when g is equal to zero, there is poor conditioning because the flow time scale is on the order of $1/(\nu k_x^2)$ while the free-surface time scale is $1/(u_\infty k_x)$. In the limit that the Reynolds number goes to zero, the ratio of these goes to infinity. This problem is easily eliminated because the free surface and the flow are totally decoupled when g is zero. We can simply take different pseudo-time steps for the flow and the free surface and get a well-conditioned problem. This is shown in the following section. For finite values of g, we are not able to obtain any valuable information from the continuous system. This limit is only studied using numerical techniques.

5.2. Discrete analysis techniques

Given this baseline understanding of the free-surface problem, we now examine the fully discrete system. We have two methods of analyzing this system. The first is a brute force technique: We Fourier transform the discrete system in ξ, which for any k_x reduces the problem to an unsteady one-dimensional problem. The eigenvalues of this problem are then found numerically. When using this technique, the results are obtained on a mesh with 100 points, k going from 0 to -99. $k = 0$ again corresponds to the free surface. At the bottom boundary, we assume that there is a point at $k = -100$ at which the values of u, v, and p are all zero. This eigenvalue problem gives a set of 301 eigenmodes, one for the flow variable at each point plus one for h at the free surface.

Usually, we find at the most four modes that exponentially decay as y goes to infinity. The remaining modes are all oscillatory. We refer to these four exponentially decaying modes as the free-surface modes. In comparison with the analytic case, we have four free-surface eigenvalues/eigenmodes instead of two

(given by the plus/minus in Eq. (34)). The two additional modes are a result of the implementation of the boundary conditions; Instead of eliminating the pressure on the free surface using the normal stress condition, we solve a dynamic equation for the pressure. This gives rise to additional free-surface modes. We call these modes the discrete free-surface modes when we need to distinguish them from the free-surface modes that have an analog in the continuous analysis.

The above technique is rather time consuming because it requires the solution of a 301-dimensional eigenvalue problem. Furthermore, when a surface parameter such as g or σ is changed, only the eigenvalues of the four free-surface modes change. The remaining eigenvalues remain unchanged. Because we are mainly interested in the free-surface modes, we use a technique similar to that used to obtain the analytic solutions: The equations are Fourier transformed in ξ and an exponential dependence in τ^* is assumed, $e^{\lambda\tau^*}$. This leaves a one-dimensional linear finite-difference problem. This finite-difference problem is written as

$$\begin{bmatrix} M-2D & D+C \\ -I & 0 \end{bmatrix}\begin{bmatrix} \hat{w}_k \\ \hat{w}_k^+ \end{bmatrix} + \begin{bmatrix} D-C & 0 \\ 0 & I \end{bmatrix}\begin{bmatrix} \hat{w}_{k-1} \\ \hat{w}_{k-1}^+ \end{bmatrix} = 0, \tag{38}$$

where each entry in the above block matrix is a 3×3 matrix. The last three equations are a shift operator so we can write the equations as a function of k and $k-1$ without explicitly referencing $k+1$. The auxiliary variables $\hat{w}_k^+$ are equal to $\hat{w}_{k+1}$. The matrices M, D, and C are given by

$$M = \Delta x\Delta y\begin{bmatrix} \frac{\lambda}{\Delta\tau^*} & 0 & 0 \\ 0 & \frac{\lambda}{\Delta\tau^*}+\frac{1}{\Delta\tau} & 0 \\ 0 & 0 & \frac{\lambda}{\Delta\tau^*}+\frac{1}{\Delta\tau} \end{bmatrix} + A_x \mathrm{i}\sin(k_x\Delta x) - \left(\frac{|A_x|}{2}+N_{xx}\right)2(\cos(k_x\Delta x)-1), \tag{39}$$

$$C = \frac{1}{2}(A_y - (N_{yx}+N_{xy})\mathrm{i}\sin(k_x\Delta x)), \tag{40}$$

$$D = -\left(\frac{|A_y|}{2}+N_{yy}\right). \tag{41}$$

Assuming the solution is of the form $\hat{w}_k = \hat{w}_0 r^k$ where $\hat{w}_0$ is the solution at the free surface and r is the geometric growth or decay factor, we again have a generalized eigenvalue problem which can be solved for r and the eigenvector, $\hat{w}_0$. In the viscous case, if we assume λ is in the left half plane, we find that three of the six eigensolutions decay as k approaches negative infinity ($r > 1$). The inviscid case is slightly more complicated and is discussed after we explain the viscous case.

Given these three eigensolutions, we then examine the free-surface equations to arrive at a compatibility condition for λ. We assume that w is a linear combination of the three decaying eigenvectors, $\hat{w}_{0,1}$, $\hat{w}_{0,2}$, and $\hat{w}_{0,3}$, with one of the three modes normalized to have magnitude unity, i.e., $\hat{w}_0 = \hat{w}_{0,1} + c_2\hat{w}_{0,2} + c_3\hat{w}_{0,3}$ and $\hat{w}_{-1} = \hat{w}_{0,1}r_1^{-1} + c_2\hat{w}_{0,2}r_2^{-1} + c_3\hat{w}_{0,3}r_3^{-1}$. These expressions are inserted into the three conservation equations at the free surface and the kinematic equation is used to eliminate any dependence on h. This gives three equations and three unknowns: c_2, c_3, and λ. The conservation equations are linear in c_2 and c_3 so these variables are eliminated to leave an equation for λ. Analytic solutions are not possible, so an initial guess is given for λ and the above procedure is combined with a Newton–Raphson iteration to find solutions. The values of λ found in this manner coincide almost exactly with the eigenvalues of the free-surface modes found using the brute-force approach. Minute differences occur because the full eigenvalue problem only has 100 points and does not extend to negative infinity.

For the inviscid case, we find one mode that decays as k goes to negative infinity, one mode that grows as k goes to negative infinity, two modes that have infinite values of r, and two modes that have zero values of r. An infinite value of r corresponds to a mode which has no coupling to the $k+1$ point in the upwind scheme. A zero value of r corresponds to a mode which has no coupling to the $k-1$ point. The decoupling

arises because the upwind scheme only involves a 2-point stencil. Generalizing the previous procedure, we choose the three modes which have $r > 1$. This corresponds to picking the decaying mode and the two modes that are uncoupled from the equations at point $k = -1$ for the solution at the free-surface point, $k = 0$. The procedure for finding the compatibility condition is identical to that for the viscous case. Results obtained in this manner again agree almost exactly with the brute force method.

5.3. Inviscid, steady flow

We begin by examining inviscid steady flow with $\Delta\tau^*_{fs} = \Delta\tau^*$. β and $\Delta\tau^*$ are given by Eqs. (29) and (28). Fig. 1 shows the eigenvalue spectrum when $k_x\Delta x = 2\pi/32$. The points marked with an $\times$ (black) are the eigenvalues of the full 301-dimensional eigenvalue problem. The solid (red) curves trace the evolution of the free-surface modes as $g\Delta x/u_\infty^2$ goes from 10^{-2} to 10^2. These curves are found using the Newton–Raphson technique for the free-surface modes. The 301-dimensional eigenvalue problem is solved with g at the upper limit of the range used to trace the curves for the free-surface modes. The value of g only affects the free-surface modes. If the end of a free-surface mode curve is marked with a $\times$ it is the large g end of the curve. The end without a $\times$ is the low g end. In some cases, it is impossible to tell from the figure because neither end of the curve is isolated from the flow eigenvalues.

We begin by explaining the flow eigenvalues (the eigenvalues plotted with an $\times$). There should be no real components to any of the eigenvalues because we basically have an undamped acoustic system. However, because the first-order upwind scheme is dissipative, there is a negative real component. The distribution of flow eigenvalues is similar to what we would see if we performed a double Fourier transform and varied k_y while keeping k_x fixed. If we look at the region close to the imaginary axis, we see three distinct branches of eigenvalues. The middle branch is convective with eigenvalues approximately equal to $ik_xu_\infty\Delta\tau^* = 0.02i$. This is the branch closest to the origin. There are many eigenvalues repeated at this point because there is no y-direction coupling of the convective modes through either the convective matrix A_y or the artificial dissipation matrix $|A_y|$. Thus the convective eigenvalues are independent of k_y. The upper and lower branches of eigenvalues along the imaginary axis are acoustic. When k_y is zero the acoustic eigenvalues are equal to $ik_x(u_\infty \pm \sqrt{u_\infty^2 + \beta})\Delta\tau^* = 0.06i, -0.04i$, which are the two points above and below the convective branch on the imaginary axis. As the eigenmodes become more oscillatory in y, there is a change in the

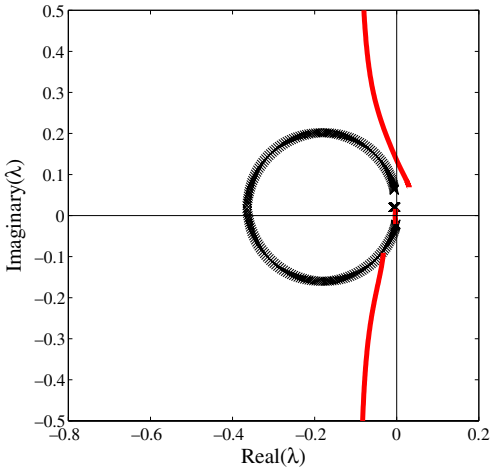

Fig. 1. Eigenvalue spectrum for inviscid, steady flow with $k_x\Delta x = \pi/16$ and $\Delta x g/u_\infty^2 = 10^{-2}$ to 10^2. The horizontal and vertical lines are the real and imaginary axis.

imaginary component of the eigenvalues because the acoustic modes are coupled in y. The amount of dissipation also increases because of the y-direction artificial dissipation terms. The most oscillatory acoustic modes in y have eigenvalues with the most negative real parts.

From the analytic solution, we expect that the eigenvalues of the free-surface modes to be strictly convective when g is small and acoustic when g is large (Eqs. (34) and (36)). One of the free-surface eigenvalues follows this behavior, moving along the imaginary axis from the convective branch to the negative imaginary acoustic branch. However, the other convective to acoustic transition is missing. Furthermore, we have two discrete free-surface modes whose imaginary components become infinitely large as g approaches infinity. The upper one of these two modes crosses the imaginary axis and becomes unstable when g approaches zero. Thus, the iteration will diverge for small values of g.

When g is small, there is little coupling between the free surface and the flow. If we examine the boundary conditions at the free surface (Eq. (15)), we see that we are trying to fix all three fluxes. Because one characteristic of A_y propagates towards the free surface, this is unstable. To overcome this problem, we modify the boundary conditions at the free surface using the kinematic condition. The modified boundary fluxes are given by

$$F = \left[0, 0, \Delta x g h_j - \frac{\sigma}{\rho \Delta x}(h_{j+1} - 2h_j + h_{j-1})\right]^{\mathrm{T}} - R_{fs,j}[\rho\beta, u_\infty, 0]^{\mathrm{T}}. \tag{42}$$

The second term of this expression uses the residual error of the kinematic condition as a convective flux through the free surface. In this way, the free surface behaves more like an outflow boundary condition where the stress is specified, but the convective fluxes are not. The final solution of the equation is unaffected because the added flux term is proportional to the residual of the kinematic condition. This modification is not necessary for finite-element formulations where the convective terms are *not* integrated by parts. In this case, the natural boundary conditions of the formulation are on the stress and not the total flux.

The results obtained with the modified fluxes are shown in Fig. 2. Now we have two of the four free-surface eigenvalues behaving as predicted by the continuous analysis. These eigenvalues move from the convective branch to the acoustic branches as g increases. We still have a problem with the imaginary component of the two discrete free-surface eigenvalues. As g increases, the magnitude of these eigenvalues

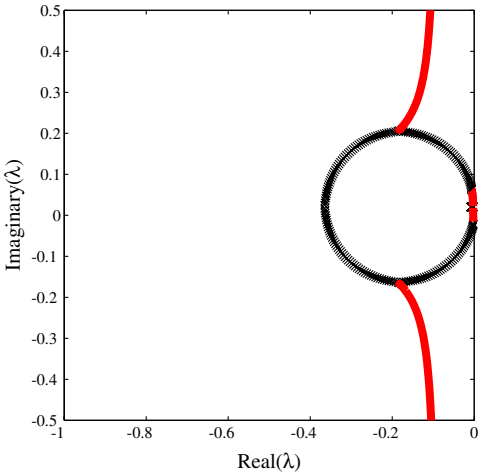

Fig. 2. Eigenvalue spectrum for inviscid, steady flow with $k_x \Delta x = \pi/16$, $\Delta x g/u_\infty^2 = 10^{-2}$ to 10^2, and modified boundary fluxes.

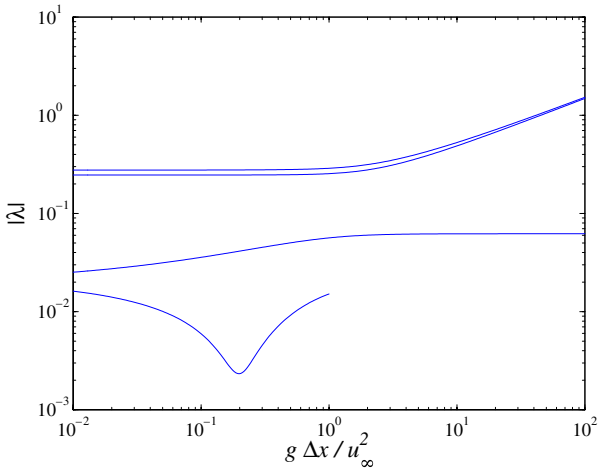

Fig. 3. Magnitude of free-surface eigenvalues for inviscid, steady flow with $k_x\Delta x = \pi/16$, $\Delta x g/u_\infty^2 = 10^{-2}$ to 10^2, and modified boundary fluxes.

increases indefinitely, which makes the system ill-conditioned. Fig. 3 shows the magnitude of the four free-surface eigenvalues as a function of $g\Delta x/u_\infty^2$. The reason that all the curves do not extend across the domain is that the Newton–Raphson solver is not always able to find the roots. This usually occurs when the free-surface mode approaches or merges with the flow modes. On the figure, the smallest magnitude eigenvalue is the one that passes from the convective branch to the lower acoustic branch. The large magnitude eigenvalues are the discrete free-surface modes. From this figure, we see that, as g increases, the discrete free-surface eigenvalues increase in magnitude with a square root dependence on g. This behavior also occurs for other values of k_x.

To overcome the stiffness associated with the discrete free-surface eigenvalues, we modify the value of $\Delta\tau_{fs}^*$. We begin by noting that in the limit that g goes to zero the kinematic condition is totally decoupled from the flow. The eigenvalues associated with the free-surface movement can be determined from the Fourier transform of Eq. (26), which is given by

$$\left(\Delta x\Delta\tau^{-1} + u_\infty \mathrm{i}\sin(k_x\Delta x) - |u_\infty|(\cos(k_x\Delta x) - 1)\right)h - \Delta x v = 0. \tag{43}$$

When g is equal to zero, the maximum free-surface eigenvalue is the coefficient of h in this expression evaluated with $k_x\Delta x = \pi$. $\Delta x/\Delta\tau_{fs}^*$ should be set equal to this value when g is zero. By experimentation, we have found that the following expression also works well when g is large:

$$\frac{1}{\Delta\tau_{fs}^*} = 2\frac{u_\infty}{\Delta x} + \frac{1}{\Delta\tau} + c\frac{g + 4\sigma/(\rho\Delta x^2)}{\sqrt{u_\infty^2 + \beta}}. \tag{44}$$

The adjustable constant, c, is given the value of 4. The justification for this is given in the following sections. Surface tension is included by noting that in Fourier space, the stress term is

$$\left(g - \frac{\sigma(2\cos(k_x\Delta x) - 2)}{\rho\Delta x^2}\right)h, \tag{45}$$

so we can again lump the effects of surface tension and gravity together. The new expression for $\Delta\tau_{fs}^*$ limits the free-surface time step in proportion to the surface stresses when g or σ is large.

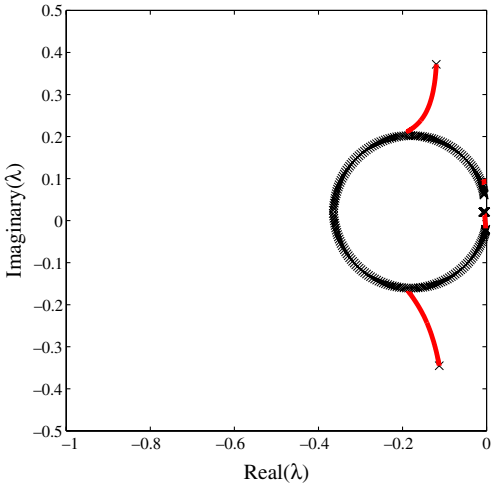

Fig. 4. Eigenvalue spectrum for inviscid, steady flow with $k_x\Delta x = \pi/16$ and $\Delta x g/u_\infty^2 = 10^{-2}$ to 10^2 with modified $\Delta\tau^*_{fs}$.

Fig. 4 shows the eigenvalue spectrum when using Eq. (44). As g increases, the two discrete free-surface eigenvalues branch off from the acoustic flow eigenvalues. In the limit of g going to infinity, they move to the position $\lambda \approx -.1 \pm 0.4\mathrm{i}$ and remain fixed. To see what happens to the other two free-surface modes, we have expanded a region of Fig. 4 around the location $(0,0)$. This is shown in Fig. 5. Unlike the previous case in which we had two eigenvalues that transitioned from convective to acoustic, in this case we have only one. This mode makes the transition from the convective branch to the lower acoustic branch as g increases. This curve should merge at both ends with the flow modes, but the Newton–Raphson iteration stops converging as these limits are approached. The second mode is associated with the kinematic condition. When g is zero, the eigenvalue is approximately $\mathrm{i}u_\infty k_x \Delta\tau^*_{fs} = 0.098\mathrm{i}$, which is shown on the figure. As g increases, it merges with the upper acoustic branch and becomes indistinguishable from the flow modes. Fig. 6 shows the magnitude of the free-surface eigenvalues as a function of g. The largest magnitude eigenvalues are the

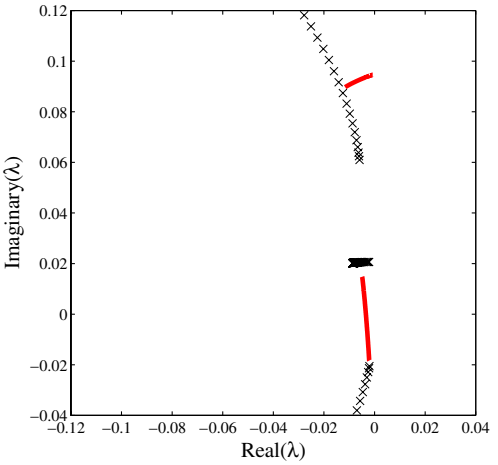

Fig. 5. Expanded view of eigenvalue spectrum for inviscid, steady flow with $k_x\Delta x = \pi/16$ and $\Delta x g/u_\infty^2 = 10^{-2}$ to 10^2 with modified $\Delta\tau^*_{fs}$.

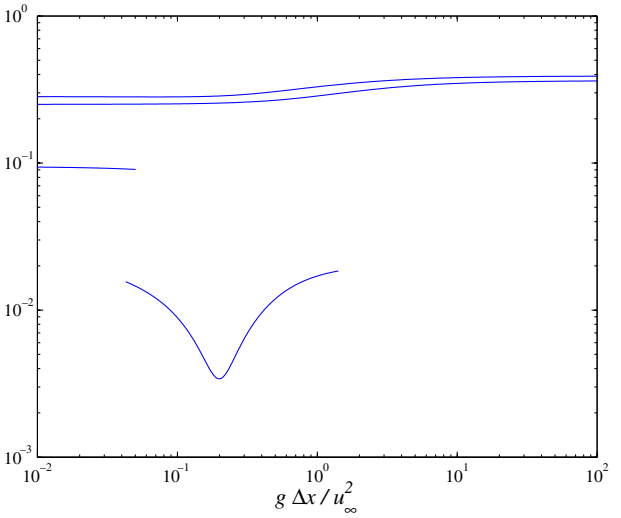

Fig. 6. Magnitude of free-surface eigenvalues for inviscid, steady flow with $k_x\Delta x = \pi/16$ and $\Delta x g/u_\infty^2 = 10^{-2}$ to 10^2 with modified $\Delta\tau^*_{fs}$.

discrete free-surface eigenvalues. This figure confirms that as g becomes large, the magnitude of these eigenvalues remains bounded.

The most important wavelengths for determining multigrid convergence are $k_x\Delta x = \pi$, and $2/3\,\pi$. These wavelengths must be damped well for multigrid to work. Fig. 7 shows the eigenvalues for the high wavenumber case, $k_x\Delta x = \pi$. The distribution of the flow eigenvalues is much different than the previous case because the upwind scheme is dissipative at high wavenumbers. The eigenvalues of the discrete free-surface modes are identifiable as the curves which have a nearly constant imaginary component equal to ± 0.3i. The large g end of the curve is the end closest to the imaginary axis. These eigenvalues are bounded and the real part is always more negative than the least negative flow eigenvalue so these modes should not limit the

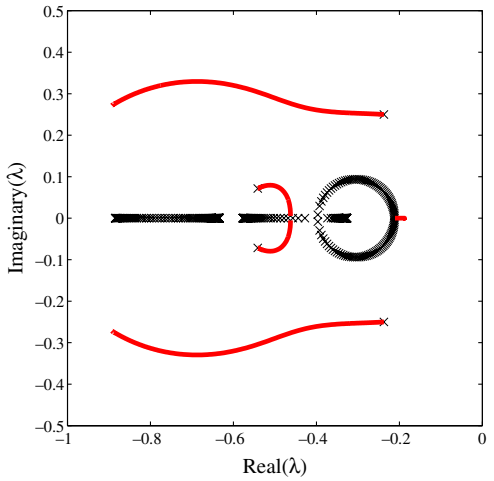

Fig. 7. Eigenvalue spectrum for inviscid, steady flow with $k_x\Delta x = \pi$ and $\Delta x g/u_\infty^2 = 10^{-2}$ to 10^2 with modified $\Delta\tau^*_{fs}$.

convergence rate. When g is equal to zero, there is only one other free-surface eigenvalue, which is located on the real axis at $\lambda = -0.19$. This eigenvalue merges with the flow eigenvalues when $g\Delta x/u_\infty^2$ is equal to one. Because this eigenvalue has a smaller negative component than any of the flow eigenvalues, it will have an effect on the convergence rate of the iteration. However, the maximum difference is small ($\lambda = -0.19$ versus $\lambda = -0.21$ for the flow eigenvalues). Furthermore, because the flow convergence rates for the inviscid case are poor, this difference will not be observable in practice.

When $g\Delta x/u_\infty^2$ is increased beyond one, two eigenvalues appear at $\lambda = -0.47$. In the limit of g going to infinity, these eigenvalues become fixed at the points marked with an $\times$ at the end of the curves originating from $\lambda = -.47$. In this limit, the convergence rate should be identical to the convergence rate of a flow without a free surface. We have also examined the eigenvalues for $k_x\Delta x = 2/3\pi$ and found a similar behavior. Thus, if we eliminated the problems with the inviscid flow preconditioner, the free-surface preconditioner would be effective for finding solutions to free-surface problems.

To justify the choice of adjustable constant, c in Eq. (44), Fig. 8 shows the evolution of the free-surface modes as c is varied over the range 0.4–100.0. $\Delta x g/u_\infty^2$ was set to 10^4 because this is the limit in which c is important. We again examine $k_x\Delta x = \pi$. The format of the plot is similar to those shown previously, with the (black) $\times$ denoting the flow eigenvalues and the (red) solid curves tracing the path of the free-surface modes as c changes. For small values of c, the position of the discrete free-surface modes is outside the range of the figure. The imaginary component of these modes is approximately ± 2i when c is 0.4. Thus, choosing too small of a value of c will cause stability problems for any explicit pseudo-time advancement scheme (e.g., the 5-stage RK method). As c is increased, the discrete free-surface modes move in toward the flow eigenvalues. When c is around 8, these modes merge with the flow eigenvalues. Beyond $c = 8$, a mode appears along the real axis and moves toward the point $(0, 0)$ with increasing c. This mode then determines the convergence rate. The real component of the other two free-surface modes remains around -0.6 and thus does not affect convergence. Fig. 9 shows the real component of the discrete free-surface modes as a function of c. The horizontal line on the figure denotes the least negative real component of all the flow eigenvalues. If we choose $c = 4$, the real component of all the free-surface modes is more negative than the least negative flow eigenvalue, and the free surface should not affect the convergence rate. The results for $k_x\Delta x = 2/3\pi$ are similar.

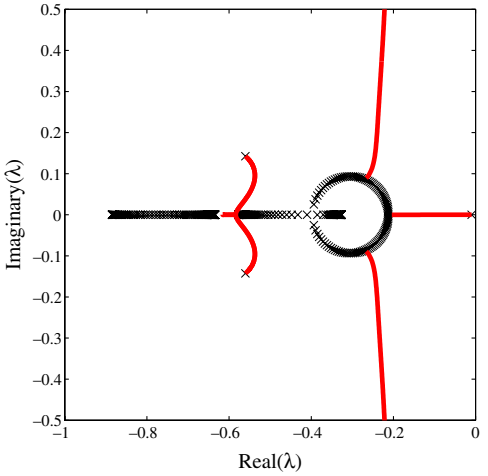

Fig. 8. Behavior of free-surface eigenvalues for inviscid, steady flow with $k_x\Delta x = \pi$, $\Delta x g/u_\infty^2 = 10^4$, and $c = 0.4$–100.

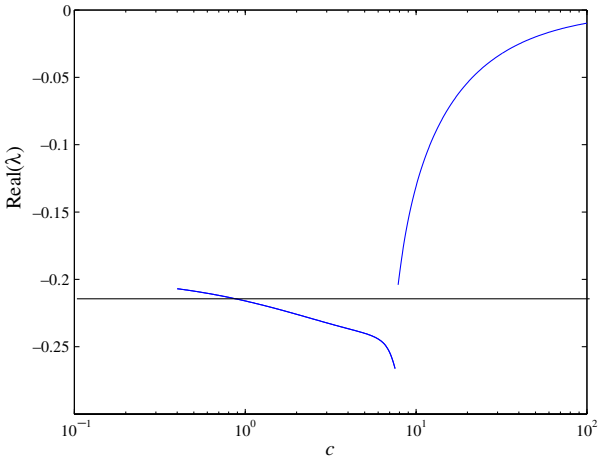

Fig. 9. Real component of free-surface eigenvalues as a function of c for inviscid, steady flow with $k_x\Delta x = \pi$ and $\Delta x g/u_\infty^2 = 10^4$.

5.4. Unsteady, inviscid flow

We next investigate unsteady flow in the limit that the CFL number goes to zero. This is done by setting u_∞ to zero. We start with $\Delta\tau^*_{fs}$ given by Eq. (44). Fig. 10 shows the eigenvalue spectrum for the case of $k_x\Delta x = \pi$. In the small g limit, we have three distinguishable free-surface eigenvalues: $\lambda = -1.0$ and the discrete free-surface modes at -0.37 ± 0.23i. The eigenvalue at -1.0, moves along the real axis and when g is O(1) merges with the flow eigenvalues at $\lambda = -0.667$. It then emerges where the flow eigenvalues cross the real axis at -0.33. With increasing g, it approaches the limiting value of -0.27. The discrete free-surface eigenvalues loop around and approach the values -0.25 ± 0.28i in the large g limit.

When $g\Delta\tau^2/\Delta x$ is less than one, none of the free-surface eigenvalues have real part that is less negative than the flow eigenvalues, and the convergence of the iteration should be unaffected by the presence of the free surface. However, for larger g, the free-surface modes move closer to the imaginary axis than the flow

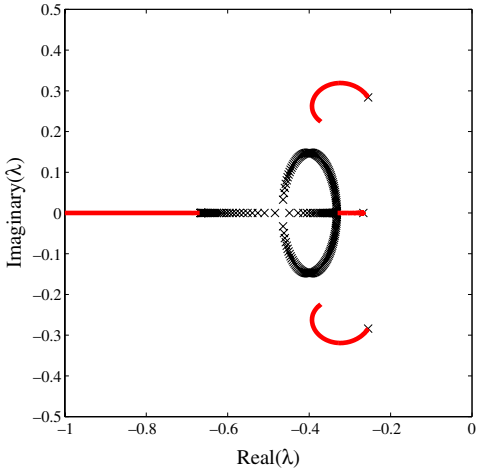

Fig. 10. Eigenvalue spectrum for inviscid, unsteady flow with $k_x\Delta x = \pi$ and $g\Delta\tau^2/\Delta x = 10^{-3}$ to 10^3.

eigenvalues. This will cause the convergence rate to decrease. Unfortunately, there is no way to eliminate this problem by modifying the free-surface time step. If we take a larger free-surface time step, the discrete free-surface eigenvalues ($\lambda = -0.25 \pm 0.28$i) move to a less negative position in the large g limit. If we take a smaller free-surface time step, the eigenvalue on the real axis moves to a less negative position. Fig. 11 shows the real part of the free-surface modes as a function of c. The choice of $c = 4$ gives the best possible result in the large g limit. In this limit, the real part of the free-surface eigenvalues is -0.27 while the least-negative real component of the flow eigenvalues is -0.33 so this should only have a moderate effect. The above behavior is also seen at longer wavelengths in x.

5.5. Stokes flow

The low Reynolds number limit is relevant when the grid based Reynolds number, $u_\infty \Delta x/\nu$ is order one or smaller. As mentioned in the discussion of the analytic results, in this limit the free-surface time scales and the flow time scales diverge. To study this limit, we cannot set u_∞ to zero because this would cause the time scale associated with the kinematic condition to go to infinity when g is zero. Instead, we let $u_\infty \Delta x/\nu$ be 1/100. The Reynolds number based on the wavenumber, k_x is also always kept less than one. When $g = 0$, Eq. (44) correctly sets the pseudo-time step for the free surface based on the convective velocity while the flow pseudo-time step is based on the viscous time scale as determined by Eq. (29).

Fig. 12 shows the evolution of the eigenvalues for $k_x \Delta x$ equal to π. When $g = 0$, there are three free-surface eigenvalues. All three are located on the real axis. The first is located at -0.95, the second is at -0.5, and the third is at -0.156, just to the right of the flow eigenvalues. Because the third eigenvalue is less negative than the flow eigenvalues it will affect convergence, but the difference is small, -0.156 versus -0.166 so it should not be a strong effect. With increasing g this eigenvalue moves towards and merges with the flow eigenvalues when $g\Delta x^3/\nu^2$ is $O(10^{-2})$. The first two eigenvalues approach each other and branch off of the real axis around the same value of $g\Delta x^3/\nu^2$. They then wrap around and approach the imaginary axis. The limiting position is -0.16 ± 0.12i. This is slightly closer to the imaginary axis than the flow eigenvalues and thus will affect convergence slightly. Unlike the unsteady case, there is no immediate penalty for using a smaller value of c. The free-surface modes move to larger imaginary values and shift to the left slightly. If too small a value of c is used, then the imaginary components of the free-surface modes will cause the explicit pseudo-time advancement scheme to become unstable.

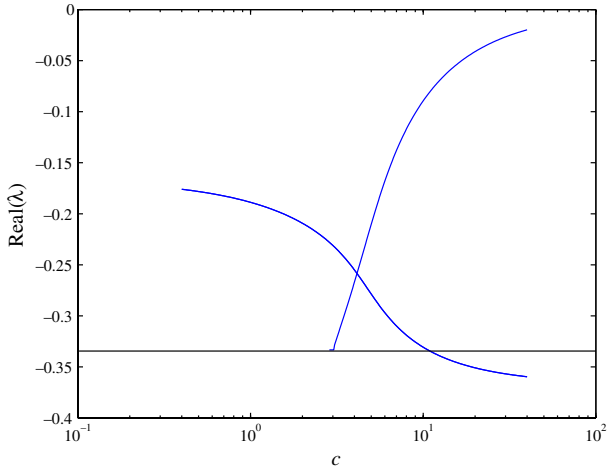

Fig. 11. Real component of free-surface eigenvalues as a function of c for inviscid, unsteady flow with $k_x \Delta x = \pi$ and $g\Delta\tau^2/\Delta x = 10^4$.

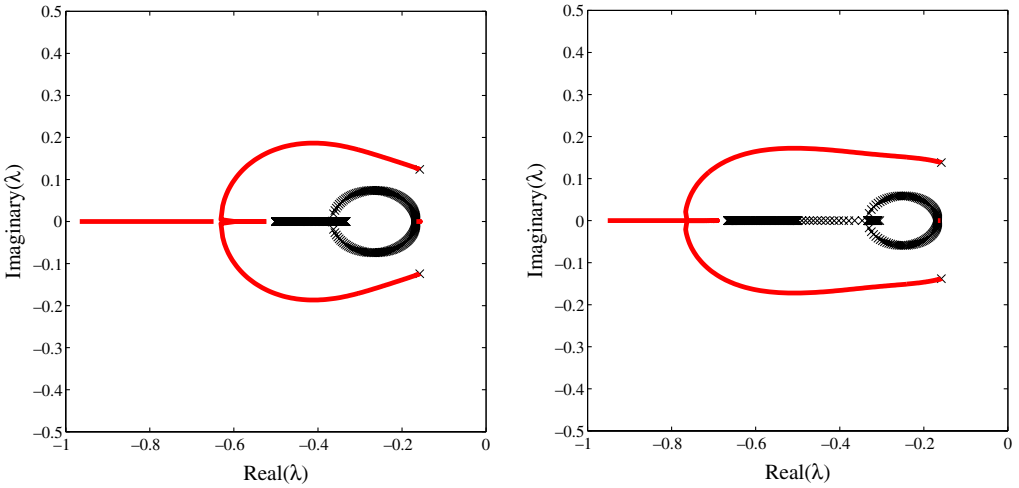

Fig. 12. Eigenvalue spectrum for viscous, steady flow with $k_x\Delta x = \pi$, $u_\infty \Delta x/\nu = 0.01$ and $g\Delta x^3/\nu^2 = 10^{-2}$ to 10^4.

5.6. Numerical tests

To verify the optimality of our preconditioner, we examine convergence rates from a SUPG *hp*-finite-element discretization of the incompressible Navier–Stokes equations. The numerical scheme is described in [10]. It is a finite-element discretization of Eq. (6) using triangular elements and a polynomial basis. Although this scheme allows higher-order polynomials, for simplicity we restrict the study to linear polynomials. When using linear polynomials, the discretization is similar to an unstructured, vertex-based, finite-volume discretization. The discrete equations are solved using multigrid. The multigrid algorithm is a full approximation and storage algorithm [23], which means that it obtains the solution to the non-linear equations not a linear approximation. The prolongation and restriction operators are the standard linear interpolation operators used on unstructured vertex based triangular meshes [23]. The relaxation scheme is given by Eq. (27) with a 5-stage RK scheme [21] to advance the solution in τ^*. Eqs. (28) and (29) for β and $\Delta\tau^*$ are generalized for use on an unstructured mesh by the following formulas:

$$\beta = 3Q_{\max}^2 + \left(\frac{\Delta_{\max}}{2\Delta\tau} + \frac{2\nu}{\Delta_{\max}}\right)^2, \tag{46}$$

$$\frac{1}{\Delta\tau^*} = 8\nu\left(\frac{1}{\Delta_{\max}^2} + \frac{1}{\Delta_{\min}^2}\right) + 2\frac{Q_{\max} + \sqrt{Q_{\max}^2 + \beta}}{\Delta_{\min}} + 2\frac{\sqrt{\beta}}{\Delta_{\max}} + \frac{1}{\Delta\tau}, \tag{47}$$

where $Q_{\max}^2$ is the maximum value of $U^2 + V^2$ for the three element vertices. $\Delta_{\max}$ is the maximum length of the three element sides. $\Delta_{\min}$ is twice the triangle area divided by $\Delta_{\max}$. A "local time-stepping" approach is used where both β and $\Delta\tau^*$ can vary across the domain. For the problem studied here, this is not important because both the flow and mesh are uniform across the domain.

At the free surface, the kinematic condition is upwinded using a SUPG approach. This is described in [10]. In the formula for $\Delta\tau^*_{fs}$, u_∞ is replaced by velocity of the flow relative to the mesh in the direction tangent to the free surface. For this problem, this is basically the horizontal velocity U. Δx in the formula for $\Delta\tau^*_{fs}$ is the length of the edges along the free surface. When we add the surface flux term given in Eq. (42), we multiply the kinematic equation residual by $[\rho\beta, U, V]$ where U and V are the horizontal and vertical

velocities evaluated at the free-surface mesh points. We also use local time-stepping for the free surface, but because the flow perturbations are small and the base flow is uniform, this is unimportant.

The test problem is a free-stream flow on a unit square. On the left side of the square is an inflow condition, and on the right side is an outflow condition. The outflow boundary condition is that the viscous stress is zero. If we use a non-reflecting boundary condition based on the characteristics of the artificial compressibility system [22] for the outflow, we get slightly better results than those presented here. The top boundary is a free-surface condition and the bottom boundary is either a slip or no-slip condition depending on whether the flow is inviscid or viscous. To understand the effect of the free surface on convergence, we compare these results to a case in which the top and bottom of the square are periodic boundary conditions. The mesh is composed of 32×32 squares that are then subdivided into triangles. Coarser meshes in the multigrid cycle have the same structure except the resolution is divided by two. Six levels of grids are used such that the coarsest grid consists of two triangles.

We examine three flow conditions: ($u_\infty = 1$, $\Delta\tau^{-1} = 0$, $\nu = 0$), ($u_\infty = 1$, $\Delta\tau^{-1} = 3200$, $\nu = 0$), and ($u_\infty = 1$, $\Delta\tau^{-1} = 0$, $\nu = 100$). These fall into the three limiting conditions investigated in the previous sections. With this resolution, the second case corresponds to a CFL number based on Δx of 1/100 and a domain length based CFL of 1/3200. The third case corresponds to a grid spacing based Reynolds number, $u_\infty \Delta x/\nu$, of 1/3200 and a domain-length based Reynolds number of 1/100. For each case, we examine three different values of g. For all three cases we examine g equal to zero. The second value of g is chosen so that the two non-zero terms in Eq. (44) are the same order of magnitude. For example in the inviscid case, g is chosen so that $u_\infty/\Delta x$ is equal to g/u_∞^2, which gives $g = 32$. In the third case, this value is increased by a factor of 100. The values of g used for inviscid flow are then $(0, 32, 3200)$. For the small CFL number limit, the values of g chosen are $(0, 1.0e5, 1.0e7)$. The same values are chosen for the low Reynolds number case.

For initial conditions we use a perturbation to free-stream that includes both high- and low-wavenumber components

$$\begin{aligned} U &= u_\infty + 1.0e-4x(1-x)(\sin(2\pi x) + \sin(16\pi x))(\sin(2\pi y) + \sin(16\pi y)), \\ V &= +1.0e-4x(1-x)(\sin(2\pi x) + \sin(16\pi x))(\sin(2\pi y) + \sin(16\pi y)), \\ P &= +1.0e-4x(1-x)(\sin(2\pi x) + \sin(16\pi x))(\sin(2\pi y) + \sin(16\pi y)). \end{aligned} \tag{48}$$

The initial position of the free surface is given by

$$y = 1 + 1.0e-4(\cos(2\pi x) + \cos(15\pi x)). \tag{49}$$

The small amplitudes of the free surface and flow perturbations are chosen because the interior points of the mesh are not allowed to move, and we want to ensure that the deformation of the cells at the free surface is not significant.

The tests are performed using a multigrid W-cycle with two five-stage RK relaxation performed after each restriction and prolongation phase of multigrid. This is a fairly large number of relaxation steps on each level of multigrid. We found that if fewer relaxations are used, some of the test cases diverge. This behavior does not occur when a doubly periodic domain is used, so there is some unfavorable interaction between multigrid and boundary conditions that is eliminated by using additional relaxation steps.

Table 1 shows the convergence factors for the problem without a free-surface and the nine free-surface cases studied. The convergence factor is the ratio of the magnitude of the residuals before and after one relaxation step. We determine a mean convergence factor by iterating until machine convergence is reached then fitting an exponential curve to a plot of the residual as a function of iteration number. In fitting the curve, we ignore the initial region of the curve where faster decaying modes are eliminated and only fit the data after a nearly constant convergence factor is reached. This convergence factor is then due to the slowest decaying mode of the iteration.

Table 1
Convergence rates for various values of g

Gravity	No free-surface	Zero	Medium	Large
Inviscid	0.977	0.977	0.977	0.977
Unsteady	0.43	0.46	0.51	0.67
Viscous	0.51	0.53	0.54	0.85

For the inviscid case, the convergence rates for zero, medium, and large gravity cases are all approximately equal and the same as found for the problem without a free-surface. Because the flow solver does a poor job in this limit, the flow eigenmodes limit the convergence rate and the free-surface modes have little effect. For the unsteady and viscous cases in the zero and medium gravity cases, the convergence rates are comparable to those without a free surface. This is in agreement with the predictions from the analysis. In the large gravity limit, the convergence rate of both the unsteady and viscous cases decrease significantly. Although some degradation in convergence is predicted by the analysis, the amount of degradation shown in the table is more than we expect, especially in the viscous case.

To determine whether the convergence can be improved in the large g limit, we perform simulations with various values of the adjustable constant c. The results are shown in Table 2. For the inviscid limit, for the reasons discussed above, the convergence rate is totally independent of c unless we choose a value less than or equal to 0.5. If we choose 0.125, the iteration diverges. This is because the imaginary component of the discrete free-surface eigenvalues becomes large and moves outside the stability region of the 5-stage RK scheme.

For the unsteady case, the convergence factor improves as c is decreased until a minimum is reached at $c = 1$. The minimum occurs at 1 instead of 4 because of differences between the SUPG finite-element formulation and the finite-volume scheme we are analyzing. Analysis of the SUPG scheme gives better agreement with the numerical tests. This shows that although we have the correct scaling for $\Delta\tau^*_{fs}$, the precise optimal value is scheme dependent. For the viscous case, we arrive at a similar conclusion.

Both the unsteady and viscous cases show non-monotonic behavior of the convergence factor for small values of c. This is a consequence of the 5-stage RK scheme. The damping rate of this scheme does not monotonically decrease as the stability boundaries are approached; there are local minima. These local minima lead to variations in convergence rate as the free-surface eigenvalues move toward the stability boundary of the scheme.

Comparing the convergence factors at $c = 1$ in Table 2, to the convergence factors at zero and medium values of g, we see that there is only a small variation in the convergence factor. Thus, the free-surface preconditioner can be used in all limits with little degradation in convergence rate. If a more effective flow solver for the inviscid case was used, we might uncover an effect of the free-surface boundary condition. However, the analysis indicates that the free-surface modes are as easily damped as the acoustic modes so this will probably not be true. Based on these results, we conclude that there is no reason to use more complex/less-physical free-surface preconditioners. By choosing the correct value of $\Delta\tau^*_{fs}$, this simple pseudo-time-advancement free-surface preconditioner can be used to obtain solutions efficiently in all limits.

Table 2
Convergence rates for various values of c in the large g limit

c	16	8	4	2	1	0.5	0.25	0.125
Inviscid	0.977	0.977	0.977	0.977	0.977	0.978	0.979	U
Unsteady	0.91	0.83	0.67	0.61	0.50	0.58	0.53	U
Viscous	0.94	0.91	0.85	0.73	0.50	0.52	0.53	0.51

6. Interfacial flows

In this section, we extrapolate the results obtained for free-surface flows to interfacial flows. The continuous problem is two, infinite depth, incompressible fluids of different density, ρ_t and ρ_b, and kinematic viscosity, ν_t and ν_b flowing parallel to each other. The subscripts t and b denote the top and bottom fluid, respectively. The fluids are separated by an interface upon which surface tension acts. In the inviscid case, the two fluids are allowed to have different free-stream velocities $u_{\infty,t}$ and $u_{\infty,b}$. Both fluids are governed by Eq. (19), however for the interfacial problem, it is more convenient to leave the momentum equations weighted by the density. At the interface, we have the condition that the jump in normal stress is balanced by surface tension. In the inviscid case, the tangential stress on both fluids at the interface is zero. In the viscous case, the jump in tangential stress is zero. These conditions are similar in form to Eqs. (17) and (18) except that when the boundary condition is a jump condition the left hand side is a jump in flux across the interface.

6.1. Discrete formulation

Because inviscid flow allows a slip velocity between the two fluids while viscous flow does not, the discrete formulations are different for the two cases. We begin with the inviscid case. Because the pressure and perturbation to the tangential velocity, u, can be discontinuous across the interface we enforce conservation of mass and tangential momentum individually for half cells above and below the interface. This is done exactly as was done for the free-surface case. Normal momentum requires more consideration because these values are related across the interface by the constraint that the normal velocity be continuous. For the linearized problem, this constraint is

$$u_{\infty,b}\frac{\partial h}{\partial x} - v_b = u_{\infty,b}\frac{\partial h}{\partial x} - v_b. \tag{50}$$

The number of unknowns in the problem should be reduced by one using this constraint. This is done by introducing a new variable at the interface

$$\bar{v} = \frac{\rho_t \Delta y_t v_t + \rho_b \Delta y_b v_b}{\Delta y_t \rho_t + \Delta y_b \rho_b}. \tag{51}$$

This is a mass-averaged velocity for the cell at the interface. v_t and v_b are the vertical flow velocities of the upper and lower fluid at the interface. We also have allowed for different mesh spacings normal to the interface, Δy_t and Δy_b.

Using the variable $\bar{v}$ and relation (50) we can write expressions for v_t and v_b in terms of h and $\bar{v}$:

$$\begin{aligned} v_b &= \bar{v} + \frac{\rho_t \Delta y_t}{\rho_t \Delta y_t + \rho_b \Delta y_b}(u_{\infty,t} - u_{\infty,b})\frac{\partial h}{\partial x}, \\ v_t &= \bar{v} - \frac{\rho_b \Delta y_b}{\rho_t \Delta y_t + \rho_b \Delta y_b}(u_{\infty,t} - u_{\infty,b})\frac{\partial h}{\partial x}. \end{aligned} \tag{52}$$

Note that when the free-stream velocities are equal, these equations simply require that the normal velocity be continuous.

Following the methodology for the free-surface problem, normal momentum conservation equations are formed for the half cell above and below the interface. The fluxes at the interface for each half cell are as yet unspecified. Substituting the relations given by Eq. (52), these equations can be written in terms of $\bar{v}$ and h instead of v_t and v_b. If we add the two equations together, we get a single evolution equation for $\bar{v}$. Furthermore, the unspecified fluxes at the interface subtract and thus result in a flux jump at the interface. This can be replaced by the stress term

$$\Delta x((\rho_b - \rho_t)gh_j - \sigma\frac{h_{j+1} - 2h_j + h_{j-1}}{\Delta x^2}),$$

which closes the formulation.

The only other place that v_t or v_b appears is the kinematic condition. This can also be written totally in terms of $\bar{v}$. Because the normal velocity must be continuous, both of the following equations hold:

$$\begin{aligned}\frac{\partial h}{\partial t} + u_{\infty,b}\frac{\partial h}{\partial x} - v_b = 0,\\ \frac{\partial h}{\partial t} + u_{\infty,t}\frac{\partial h}{\partial x} - v_t = 0.\end{aligned} \tag{53}$$

Mass averaging both equations in a manner similar to that shown in Eq. (51) gives

$$\frac{\partial h}{\partial t} + \bar{u}_\infty\frac{\partial h}{\partial x} - \bar{v} = 0, \tag{54}$$

where $\bar{u}_\infty$ is the mass-averaged free-stream velocity calculated in the same way as $\bar{v}$. This eliminates any explicit dependence on v_t or v_b, which shows that v_t and v_b are auxiliary variables not needed to describe the system's evolution. It also shows that the characteristic velocity for the interface is the mass-averaged free-stream velocity, $\bar{u}_\infty$.

For the viscous case, the formulation is simpler because both u and v are continuous at the interface. We can then add the half cells above and below the interface for normal and tangential momentum to reduce the dimension of the system. The stress jumps at the interface can then be replaced using the jump equations. The pressure is discontinuous so discrete continuity is enforced individually for the half cell above and below the interface.

6.2. Preconditioning

The flow preconditioner remains the same as in previous cases. The only difference is that the preconditioner for the momentum equations has an additional density weighting because we did not divide the momentum equations by the density. β and $\Delta\tau^*$ are chosen separately for each fluid. For any variable at the interface that is continuous ($\bar{v}$ in the inviscid case and u and v in the viscous case), a mass-averaged time step is used

$$\left(\frac{\rho_t\Delta x\Delta y_t}{\Delta\tau_t^*} + \frac{\rho_b\Delta x\Delta y_b}{\Delta\tau_b^*}\right)\frac{\partial w_{j,0}}{\partial\tau^*} + R_{j,0}(w) = 0. \tag{55}$$

When ρ_t is zero, this gives exactly the same result as in the free-surface case. When both fluids are the identical, it gives the same results as for a cell in the interior of the domain. Thus, at least in these two limits this form is correct.

Similar to the free-surface case, the residual of the kinematic condition is used as a convective flux through the interface of the form

$$-R_{fs,j}[\rho\beta, \rho u_\infty, 0]^T. \tag{56}$$

This flux is added to the half cell below the interface using $\rho\beta = \rho_b\beta_b$ and $\rho u_\infty = \rho_b u_{\infty,b}$ and subtracted from the half cell above the interface using $\rho\beta = \rho_t\beta_t$ and $\rho u_\infty = \rho_t u_{\infty,t}$. For the viscous case, the horizontal momentum term is added and subtracted from the same equation because tangential velocity is continuous across the interface. If there is no density change across the interface, these terms cancel. If there is a density change, a source term of magnitude $-R_{fs,j}(\rho_b - \rho_t)u_\infty$ is added.

The interfacial time step, $\Delta\tau^*_{fs}$, is given by

$$\frac{1}{\Delta\tau^*_{fs}} = 2\bar{u}_\infty/\Delta x + \Delta\tau^{-1} + c\frac{(\rho_b - \rho_t)g + 4\sigma/\Delta x^2}{\rho_t\sqrt{u^2_{\infty,t} + \beta_{fs,t}} + \rho_b\sqrt{u^2_{\infty,b} + \beta_{fs,b}}}. \tag{57}$$

When g and σ are zero, the interface is decoupled from the flow, and the above form should be correct based on the fact that $\bar{u}_\infty$ is the characteristic velocity for the interface. When ρ_t is zero, the free-surface results are recovered. The one questionable limit is when the surface stresses are large and the artificial speeds of sound ($\sqrt{u^2_\infty + \beta}$) are much different in each fluid. There are other ways to average the artificial speeds of sound such as $(\rho_t/\sqrt{u^2_{\infty,t} + \beta_t} + \rho_b/\sqrt{u^2_{\infty,b} + \beta_b})/(\rho_t + \rho_b)^2$ which can give much different results.

To test this limit, we examine the following case: $k_x\Delta x = \pi$, $u_{\infty,t} = u_{\infty,b} = 1$, $\rho_t = \rho_b = 1$, $\mu_b = 1$, $\mu_t = 1000$, and $\sigma = 1000$. Because of the large difference in viscosity of the two fluids, the values of β are much different and thus so are the artificial speeds of sound. For the interface problem, we have only implemented the brute force eigenvalue technique so we only show the eigenvalues for this single condition. The eigenvalue problem has approximately 600 degrees of freedom because the top and bottom fluids each contain 100 points. Fig. 13 shows the eigenvalue spectrum. The conditioning of the system is as good as the free-surface cases, so this is the right form for the interface preconditioner. For the second averaging method mentioned above, two eigenvalues approach zero causing the system to be ill-conditioned. This result also confirms that the mass-averaged time step for the flow variables at the interface is correct; the time steps of the two fluids are very different so if this average was incorrect, we would see poor conditioning.

Based on comparison to results of the previous sections, the interfacial preconditioner should be correct when we have the same fluids on top and bottom, when the density of the upper fluid goes to zero, and, based on Fig. 13, when the time scales of the two fluids are very different. Because we have only implemented the brute force method for finding the eigenvalue spectrums, we confirm these conclusions using numerical tests.

6.3. Numerical tests

To validate the interfacial preconditioner, we use a similar problem to that used for the free-surface validation. In this case however, we have two square domains that are vertically adjacent. The boundary

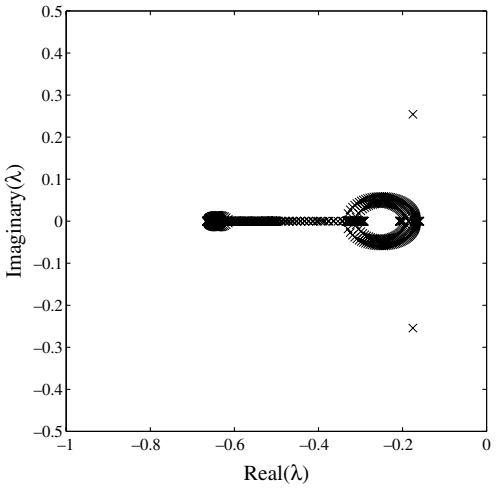

Fig. 13. Eigenvalue spectrum for viscous, steady interfacial flow with $k_x\Delta x = \pi$, $u_{\infty,t} = u_{\infty,b} = 1$, $\rho_t = \rho_b = 1$, $\mu_b = 1$, $\mu_t = 1000$, and $\sigma = 1000$.

between the domains is the interface. The code we are using for the numerical tests was written for viscous interfacial flows and thus does not allow a jump in slip velocity at the interface. For this reason, we modify the cases we study. We again study three limits, but instead of setting the viscosity to zero, we have a finite viscosity in all cases. In addition, we limit the study to problems in which the upper and lower fluid have the same free-stream velocity. This is done to be consistent with the no-slip condition across the interface and also because a jump in free-stream velocity causes physical instabilities. Because gravity has no effect when the density of the top and bottom fluid is identical, we use surface tension to study the large stress limit. Periodic boundary conditions are used because all the problems are viscous and there is no possibility of non-uniqueness of the solution due to slip. It is also easier for us to apply surface tension in the periodic problem. We use the same initial conditions as for the free-surface cases. The only change is that in the medium and large surface tension limits, we reduce the amplitude of the free-surface perturbation to 10^{-6} and 10^{-8}, respectively. With large values of surface tension, the smaller perturbation is necessary to avoid interfacial oscillations greater than the grid size. The only other difference from the free-surface case is that the adjustable parameter, c, is given the value of 1 which matches the optimum found from the free-surface tests.

Table 3 shows the results for the inviscid limit. Six cases are studied. For all of the cases, the Reynolds number based on the grid scale for both the upper and lower fluid is 100. The Reynolds number based on the domain length is then 3200. The first three cases correspond to the zero, medium, and large stress limits for fluids that have equal densities and viscosities. The second three cases have a density ratio of 1/100. For the second three cases, the viscosity of the upper fluid was reduced in the same ratio as the density such that the Reynolds number of the upper flow is kept the same. The viscosity is of secondary importance in determining the convergence factor because the flow is high Reynolds number.

Examining the first three cases, we see that we have convergence factors in all three limits that are slightly better than both the inviscid case with no surface and the free-surface problem. This is because we have a finite viscosity. Viscosity provides damping on the convective modes which improves the convergence rate. We see almost no difference between the three different stress cases because the convergence is again limited by the flow solution. For the last three cases, the convergence factors are almost indistinguishable from the first three. Thus, the density ratio change of 1/100 has almost no impact on the convergence factor. This confirms that the density weighted averages of the flow and interfacial time steps are correct in the inviscid limit.

Table 4 shows the convergence factors for the unsteady limit. The Reynolds number is kept the same as in the inviscid case. The CFL number is 1/100 based on the grid scale and 1/3200 based on the domain length. We again study the three limits of zero, medium, and large stress based on the ratio of the unsteady and stress terms in Eq. (57). As in the previous case, a density ratio of 1 and 1/100 is studied. The convergence factors show very little dependence on the density ratio again confirming that the density-weighted averages are correct. For the low and medium stress cases, the convergence rates are nearly the same, but there is a noticeable decrease in convergence rate in the large stress limit. This is the most difficult limit to get good convergence rates because, as shown in Fig. 10 for the free-surface case, there is a local

Table 3
Interfacial flow convergence factors in the inviscid limit

ρ_t/ρ_b	μ_t/μ_b	$\rho_b u_\infty \Delta x/\mu_b$	$u_\infty \Delta\tau/\Delta x$	$\sigma/(\rho_b u_\infty^2 \Delta x)$	Factor
1	1	100	0	0	0.963
1	1	100	0	32	0.961
1	1	100	0	3200	0.961
1/100	1/100	100	0	0	0.964
1/100	1/100	100	0	1	0.958
1/100	1/100	100	0	100	0.958

Table 4
Interfacial flow convergence factors in the unsteady limit

ρ_t/ρ_b	μ_t/μ_b	$\rho_b u_\infty \Delta x/\mu_b$	$u_\infty \Delta\tau/\Delta x$	$\sigma\Delta\tau^2/(\rho_b \Delta x^3)$	Factor
1	1	100	1/100	0	0.48
1	1	100	1/100	1	0.51
1	1	100	1/100	100	0.65
1/100	1/100	100	1/100	0	0.47
1/100	1/100	100	1/100	1	0.57
1/100	1/100	100	1/100	100	0.65

Table 5
Interfacial flow convergence factors in the viscous limit

ρ_t/ρ_b	μ_t/μ_b	$\rho_b u_\infty \Delta x/\mu_b$	$u_\infty \Delta\tau/\Delta x$	$\sigma/(u_\infty \mu_b)$	Factor
1	1	1/3200	0	0	0.58
1	1	1/3200	0	1	0.43
1	1	1/3200	0	100	0.48
1	1/100	1/3200	0	0	0.59
1	1/100	1/3200	0	1	0.47
1	1/100	1/3200	0	100	0.50

minimum in the real component of the free-surface eigenvalues. This minimum is less negative than the flow modes so the convergence rates are affected by the presence of a free-surface or interface.

The results for the viscous case are shown in Table 5. For all cases, the Reynolds number based on the grid scale and the lower fluid properties is 1/3200. The Reynolds number based on the domain length is 1/100. For the first three cases, the density and viscosity ratio is 1 and the upper and lower fluid conditions are the same. For the second case, the density ratio is kept at one while the upper fluid viscosity is decreased by a factor of 100. This makes the Reynolds number based on the upper fluid properties 1/32 when using the grid scale and 1 when using the domain length. Because we are in the low Reynolds number limit, the density has a secondary effect on converge and we do not investigate the effect of density ratio. Examining the results, we see that the convergence rates are nearly independent of viscosity ratio. We also see that the results are very good for the medium and large stress limit. The slowest converging case is the zero stress limit. For the free-surface case, in the low stress limit one free-surface eigenvalue becomes slightly less negative than the flow eigenvalues slowing the convergence rate (Fig. 12 and discussion). Although this did not have a strong effect on the convergence rates for the free-surface problem, it seems to have a more significant effect in the interfacial case. However, the convergence rate is still very good which gives final confirmation that the interface preconditioner is correct.

7. Conclusions

We have investigated preconditioners for arbitrary-Lagrangian–Eulerian incompressible free-surface and interfacial flow simulations. The free-surface preconditioner is based on a quasi-physical movement of the free surface in a "pseudo-time" iteration. We discovered that for this to be successful the surface fluxes must be modified to have a convergent iteration. The modification involves using the error in the kinematic condition as an artificial convective flux through the surface. We also found that there are surface eigenvalues that have no counterpart in the continuous problem and these eigenvalues can cause the system to become ill-conditioned when surface tension or gravity becomes large. This problem can be overcome by using a iterative time step for the advancement of the free-surface position that is independent of the flow

time-step. We have determined the proper scaling for this time step, such that convergence rates comparable to a simulation without a free surface can be obtained for all combinations of flow and free-surface parameters. Prior to this analysis, many different approaches for solving free-surface problems have been tried, but none have been demonstrated to be applicable for all flow conditions.

We also extended the free-surface preconditioner for application to interfacial flows. This extension involved calculating iterative time steps and artificial speeds of sound using a mass averaging technique for the interfacial grid cells. This technique produces the correct results in the limits of identical fluids or a free-surface flow. We also verified that it produces well-conditioned results when the characteristic time scales of the two fluids are very different. As for the free-surface case, this is the first time that a preconditioner for interfacial flow has been identified that works well under all flow conditions.

References

[1] J. Farmer, L. Martinelli, A. Jameson, Fast multigrid method for solving incompressible hydrodynamic problems with free surfaces, AIAA Journal 32 (6) (1994) 1175–1182.
[2] Y. Tahara, F. Stern, A large-domain approach for calculating ship boundary layers and wakes and wave fields for nonzero froude number, J. Comp. Phys. 127 (2) (1996) 398–411.
[3] D.S. Dandy, L.G. Leal, Buoyancy-driven motion of a deformable drop through a quiescent liquid at intermediate Reynolds numbers, J. Fluid Mech. 208 (1989) 161–192.
[4] B.T. Helenbrook, C.F. Edwards, Quasi-steady deformation and drag of uncontaminated liquid drops, Int. J. Multi-Phase Flows. 28 (2002) 1631–1657.
[5] R.E. Nickell, R.I. Tanner, B. Caswell, The solution of viscous incompressible jet and free-surface flows using finite-element methods, J. Fluid Mech. 65 (1974) 189–206.
[6] C.Y. Loh, H. Rasmussen, A numerical procedure for viscous free surface flows, Appl. Num. Math. 3 (1987) 479–495.
[7] L.-W. Ho, E.M. Rönquist, Spectral element solution of steady incompressible viscous free-surface flows, Finite Elements Anal. Design 16 (1994) 207–227.
[8] D. Pan, Y.-S. Yang, C.-H. Chang, Computation of internal flow with free surfaces using artificial compressibility, Numerical Heat Transfer, Part B 33 (4) (1998) 119–134.
[9] I. Robertson, S. Sherwin, Free-surface flow simulation using hp/spectral elements, J. Comp. Phys. 155 (1999) 26–53.
[10] B.T. Helenbrook, A two-fluid spectral element method, Comp. Meth. Appl. Mech. Eng. 191 (2001) 273–294.
[11] B.R. Hodges, R.L. Street, On simulation of turbulent nonlinear free-surface flows, J. Comp. Phys. 151 (1999) 425–457.
[12] W.-T. Tsai, A numerical study of the evolution and structure of a turbulent shear layer under a free surface, J. Fluid Mech. 354 (1998) 239–276.
[13] S. Ohring, H.J. Lugt, Interaction of a viscous vortex pair with a free surface, J. Fluid Mech. 227 (1991) 47–70.
[14] F.M. Orr, L.E. Scriven, Rimming flow: Numerical simulation of steady, viscous, free-surface flow wih surface tension, J. Fluid Mech. 84 (1978) 145–165.
[15] G. Ryskin, L.G. Leal, Numerical solution of free-boundary problems in fluid mechanics: Part 1: The finite-difference technique, J. Fluid Mech. 148 (1984) 1–17.
[16] A.J. Chorin, A numerical method for solving incompressible viscous flow problems, J. Comput. Phys. 2 (1967) 12–26.
[17] E. Turkel, Preconditioned methods for solving the incompressible and low speed compressible equations, J. Comp. Phys. 72 (1987) 277–298.
[18] J.D. Ramshaw, V.A. Mousseau, Accelerated artificial compressibility method for steady-state inompressible flow calculations, Comput. & Fluids 18 (4) (1990) 361–367.
[19] B.T. Helenbrook, Preconditioning for incompressible flow simulations in all limits, in preparation.
[20] A.N. Brooks, T.J.R. Hughes, Streamline upwind/Petrov-Galerkin formulations for convection dominated flows with particular emphasis on the incompressible Navier-Stokes equations, Comp. Meth. Appl. Mech. Eng. 32 (1982) 199–259.
[21] L. Martinelli, Calculations of viscous flow with a multigrid method, Ph.D. thesis, Princeton University, Princeton, NJ (October 1987).
[22] A. Belov, A new multigrid-driven algorithm for unsteady incompressible flow calculations on parallel computers, Ph.D. thesis, Princeton University (June 1997).
[23] D.J. Mavriplis, Multigrid techniques for unstructured meshes, Tech. Rep. 95-27, ICASE (April 1995).